



● Original Contribution

A CLOSED-FORM DIFFERENTIAL FORMULATION FOR ULTRASOUND SPATIAL CALIBRATION: MULTI-WEDGE PHANTOM

MOHAMMAD NAJAFI,* NARGES AFHAM,* PURANG ABOLMAESUMI,* and ROBERT ROHLING*[†]

*Department of Electrical and Computer Engineering, University of British Columbia, Vancouver, Canada; and [†]Department of Mechanical Engineering, University of British Columbia, Vancouver, Canada

(Received 7 November 2013; revised 5 March 2014; in final form 6 March 2014)

Abstract—Calibration is essential in freehand 3-D ultrasound to find the spatial transformation from the image coordinates to the sensor coordinate system. Calibration accuracy has significant impact on image-guided interventions. We introduce a new mathematical framework that uses differential measurements to achieve high calibration accuracy. Accurate measurements of axial differences in ultrasound images of a multi-wedge phantom are used to calculate the calibration matrix with a closed-form solution. The multi-wedge phantom has been designed based on the proposed differential framework and can be mass-produced inexpensively using a 3-D printer. The proposed method enables easy, fast and highly accurate ultrasound calibration, which is essential for most current ultrasound-guided applications and also widens the range of new applications. The precision of the method using only a single image of the phantom is comparable to that of the standard N-wire method using 50 images. The method can also directly take advantage of the fine sampling rate of radiofrequency ultrasound data to achieve very high calibration accuracy. With 100 radiofrequency ultrasound images, the method achieves a point reconstruction error of 0.09 ± 0.39 mm. (E-mail: rohling@ece.ubc.ca) © 2014 World Federation for Ultrasound in Medicine & Biology.

Key Words: Ultrasound, Calibration, Closed-form, Multi-wedge, Differential.

INTRODUCTION

Ultrasound is a tolerable, portable, inexpensive and real-time modality that can produce 2-D and 3-D images. Therefore it is a valuable intra-operative imaging modality to guide surgeons aiming to achieve higher accuracy of the intervention and improve patient outcomes.

In all the clinical applications that use freehand tracked ultrasound, the challenge is to precisely locate the ultrasound image pixels with respect to a tracking sensor on the transducer. This process is called *spatial calibration*, and the objective is to determine the spatial transformation between the ultrasound image coordinates and a coordinate system defined by the tracking sensor on the transducer housing. Occasionally, it is also required to perform the calibration intra-operatively, which poses other important challenges. Intra-operative calibration requires a fast, robust and easy procedure using a calibration device that is portable, small and compatible with

the sterile environment (Peterhans et al. 2010). Even an error of about a degree can cause points to be located several millimeters from their true positions (Gee et al. 2005). One example is ultrasound guided out-of-plane needle insertion (Najafi and Rohling 2011), where 0.5° error in the needle trajectory's angle could result in more than 5 mm error in the intersection point. Even higher accuracy is required in an in-plane needle insertion procedure.

The ultrasound calibration problem has been investigated over the last two decades. Most of the calibration techniques are based on imaging an artificial object with known geometric parameters. Prior knowledge of the phantom, along with ultrasound images of the phantom, is required to calculate the calibration parameters. The phantom can be as simple as a fixed point target which can be constructed as a bead (Amin et al. 2001; Detmer et al. 1994), crossed-wires (Melvær et al. 2011; Trobaugh et al. 1994; Yaniv et al. 2011) or the center of a sphere (Brendel et al. 2004). Alternatively, the phantom can be a fixed plane as in the single-wall method (Najafi et al. 2012b; Prager et al. 1998; Yaniv et al. 2011) or in its variant called the Cambridge phantom (Prager et al.

Address correspondence to: Robert Rohling, Department of Electrical and Computer Engineering, University of British Columbia, 3059-2332 Main Mall, Vancouver, BC V6T 1Z4, Canada. E-mail: rohling@ece.ubc.ca

1998). Another class of calibration phantoms consists of thin wires, usually with N- or Z-shaped patterns (Boctor et al. 2004; Chen et al. 2009; Pagoulatos et al. 2001; Peterhans et al. 2010). Another approach is based on registration of 2-D ultrasound images with the 3-D model of the phantom (Bergmeir et al. 2009; Blackall et al. 2000; Lange et al. 2011). Some calibration methods are based on precise manual alignment of the ultrasound image with a thin planar phantom (Gee et al. 2005; Lindseth et al. 2003). There are also some methods that do not require a phantom and use a calibrated stylus (Hsu et al. 2008; Khamene and Sauer 2005; Muratore and Galloway 2001) or use changes in speckle from transducer movements (Boctor et al. 2006b). Detailed reviews, comparison of different calibration methods and a summary of various validation techniques can be found in survey papers by Mercier et al. (2005) and Hsu et al. (2009).

Calibration methods can also be categorized as either iterative optimization techniques (e.g., Detmer et al. 1994; Melvær et al. 2011; Prager et al. 1998) or closed-form solutions (e.g., (Boctor et al. 2004; Chen et al. 2009; Najafi et al. 2012b)). Iterative methods are subject to sub-optimal local minima, are sensitive to initial estimates and, therefore, are less robust in general than closed-form solutions (Eggert et al. 1997). They also typically require more input data to achieve the same level of accuracy.

Despite all these efforts, it is not easy to find a method for ultrasound calibration that is fast and easy to perform while at the same time being highly accurate. This may adversely affect the result of ultrasound-guided interventions and possibly limit the scope of new applications. Accurate, absolute localization of phantom features in ultrasound images is the biggest challenge in the calibration process (Lange et al. 2011) and is the limiting factor in increasing the accuracy of calibration.

One reason is the blurry appearance of features caused by the finite resolution of the ultrasound images and the presence of noise. There are also image formation errors resulting from speed of sound variations, refraction and a finite beam width, all of which contribute to distortions in the shape of the depicted features.

Finite resolution of the ultrasound and imaging artifacts, for example, causes small point-shaped objects to appear as short lines in the ultrasound images (Chen et al. 2009); therefore, a cross section of a wire in an ultrasound image does not appear in the shape of a circle, but rather as an asymmetric cloud with a width of several pixels. This makes it very challenging to accurately localize the actual intersection point. The finite beam width also affects the accuracy of feature localization of planar objects (Prager et al. 1998). A plane appears in the ultrasound image as a line with a thickness related

to the beam width and plane orientation. Unlike point features, the shape of the line remains unchanged along the line as long as the plane's inclination relative to the beam direction is not high.

To improve accuracy, the need for absolute localization of the calibration phantom features should be eliminated. We propose to achieve this by using a differential measurement of the relative distance between two image features. Advancements in differential measurements for ultrasound motion tracking in recent years have enabled accurate measurements of the relative locations of phantom features. This accuracy can be as high as a few microns when radiofrequency (RF) ultrasound data are used (Walker and Trahey 1995).

The differential measurement can be especially accurate when the shapes of the features are very similar. Because the appearance of a wire varies with depth in the image (Chen et al. 2009), it is more difficult to perform accurate measurements of the distance difference of point features unless only pairs of features with similar shapes are selected. Planar phantoms, on the other hand, are ideal because the plane appears as a line with uniform thickness. In fact, echo RF pulses in all RF scan lines exhibit a similar pattern because they all experience the same physical situation except for a variation in the ultrasound focus (and, therefore, beam width), which slightly varies according to the depth. The relative axial distance of line features can be measured as the relative shift between echo RF pulses and is, therefore, a differential measurement. This measurement can be performed very accurately, especially with RF data. Redundancy of measurements, because of the presence of many scan lines, is another advantage of planar objects over wires. Redundancy allows averaging of measurements, which can also reduce error from measurement noise.

Closed-form calibration based on measurements of the relative pose of two different images using hand-eye coordination technique has been proposed before (Bergmeir et al. 2009; Boctor et al. 2004). Although relative measurements have an inherent advantage, accurate estimation of the relative 3-D poses of 2-D ultrasound images remains a challenge. This work is based on in-plane differential measurements which can also directly take advantage of the fine sampling rate of RF ultrasound data to achieve high measurement accuracy. Moreover, wedges have been used for alignment and calibration before (Afsham et al. 2011; Boctor et al. 2006a). The proposed multi-wedge phantom has been specifically designed and optimized for closed-form differential calibration.

Our aim was to make calibration more reliable for day-to-day clinical use by reducing the calibration error while keeping the calibration procedure as fast and simple as possible and suitable for intra-operative use.

Therefore, by bringing down the calibration mean error, we ensure that worst-case calibration error in any given day is still acceptable. Based on our review of calibration and observations on the key aspects limiting calibration accuracy, we have tried to reduce feature localization (*i.e.*, segmentation) error significantly by introducing a novel differential measurement technique. The proposed designed phantom is small, inexpensive to manufacture and can be easily used in clinical and surgical environments.

Our first work was a closed-form differential calibration method using a single-wall phantom (Najafi *et al.* 2012b). Next, we developed a multi-wedge phantom differential calibration method (Najafi *et al.* 2012a). In Najafi *et al.* (2012a), we presented the proposed multi-wedge closed-form solution. Here we have extended the work by developing a thorough mathematical derivation of the closed-form solution along with a sensitivity analysis of the method. Also, the results are compared with those of the standard N-wire method (Chen *et al.* 2009) in terms of the point reconstruction accuracy (PRA) test using a stylus and the calibration reproducibility (CR) test. Moreover, a fully automatic segmentation algorithm has been developed and tested. Overall, accuracy has been improved over the earlier work.

In summary, this article describes a novel calibration method based on differential measurements within ultrasound image features to reduce segmentation error. A mathematical framework was developed to calculate, in closed form, the calibration parameters using these differential measurements. The proposed framework is based on the axial and lateral imaging vectors, which also allows the incorporation of speed of sound scale variation as another unknown in the calibration formulation. The pose of the ultrasound imaging plane can be estimated from a single image of the multi-wedge phantom with the proposed method using differential measurements. This closed-form solution eliminates the need for an iterative optimization method. The multi-wedge phantom is composed of several planes (or wedges) and takes advantage of differential technique. In this work, the optimal design of the wedge angles to achieve high-accuracy measurements has been investigated.

Calibration will be described for linear array transducers for simplicity, although the method can be easily extended to curvilinear transducers by incorporating the known sector angle and radius in the geometric formulation.

METHODS

As explained before, planar objects are ideal for accurate differential measurements, because echoes from different portions of a plane with similar beam angle

will have similar echo RF signatures. To find the full pose of the ultrasound image plane, a single measurement is not enough. At least five planes are required to solve for all degrees of freedom of the calibration problem, including speed of sound variation scale (see Rotation Parameters). Therefore, a phantom composed of five planes has been proposed. This multi-wedge phantom will be seen in the ultrasound image as five line segments (Fig. 1). Based on differential measurements of these features in the image, it is possible to calculate most of the pose parameters of the ultrasound image relative to the phantom coordinate system. An absolute measurement within the same image is still needed for one translation vector.

For an independent accuracy evaluation of the calibration results, a set of two non-overlapping N-wires with known geometry and location relative to the wedges were incorporated into the phantom. This double N-wire phantom (Chen *et al.* 2009) was used for comparison purposes.

The phantom (Fig. 2) was precisely manufactured with the Objet30 desktop 3-D printer (Objet Geometries, Billerica, MA, USA). The 3-D printer has 28-mm precision, and the construction cost is relatively low (<\$200).

In our calibration experimental setup, a Sonix-TOUCH ultrasound machine (Ultrasonix, Richmond, BC, Canada) was used for ultrasound imaging. An L transducer with 7.2-MHz center frequency operating at 10 MHz in our experiments was used for imaging. The

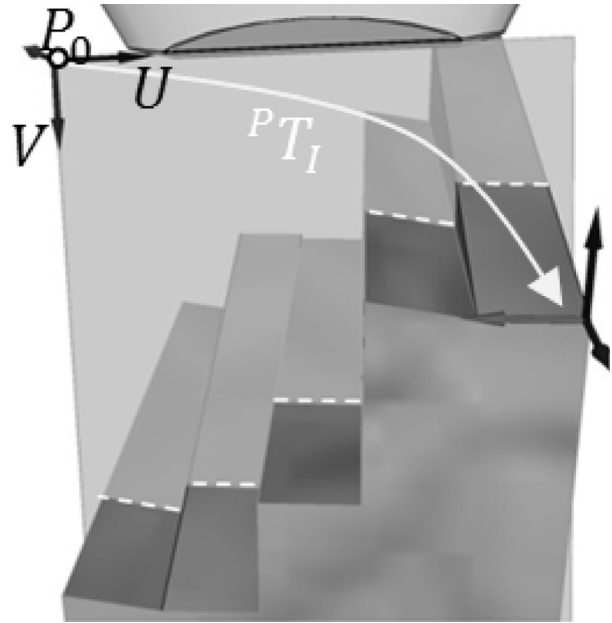


Fig. 1. Multi-wedge phantom model comprising five different planes. The *dashed line* indicates the ultrasound image intersection line segments. The transformation from image to phantom coordinate system is calculated with a closed-form solution.

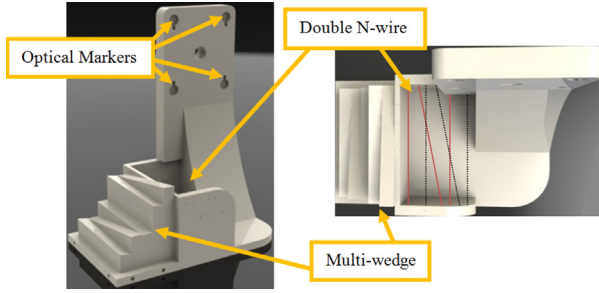


Fig. 2. Manufactured multi-wedge phantom with optical markers and a double N-wire phantom incorporated into it.

transmit focus count was set to 1, and the focus depth chosen was 35 mm to ensure that it is near to, or slightly lower than, all the line segments. Using the Ultrasonix provided focus curves; this corresponds to F8.8 on transmit and starts at F5.8 on receive (dynamic).

An Optotrak Certus optical tracker (Northern Digital, Waterloo, ON, Canada) was used to track the transducer and the phantom. Note that the Optotrak was used here because of high accuracy, but other trackers could also be used with the proposed calibration method. Random errors from less accurate stereo trackers may be accommodated by the use of a redundant measurement algorithm. To track an object with this tracker, a set of active markers with a rigid arranged geometry (rigid body) were attached to the object. The tracker measures the relative transform from an arbitrary coordinate system defined on the rigid body to the tracker's reference coordinate system.

In our experimental setup, NDI's standard four-marker sensor (rectangular rigid body configuration) was used to track both the phantom and the probe. A 4-marker sensor was also precisely incorporated into the design of the phantom to track the coordinate system of the wedges. Based on the computer-aided design (CAD) model of the phantom and the 4-marker sensor, the location of the wedges relative to the 4-marker sensor's coordinate system is known. This has been further validated with a calibrated stylus to make sure the 4-marker sensor has been precisely attached to the phantom's body.

In the calibration procedure, the coordinate systems defined on the markers' rigid bodies on both the phantom and transducer are simultaneously acquired from the tracker. Therefore, the coordinate system of the phantom's wedges, P , with respect to the tracker's reference coordinate system, R , is always known. The coordinate system on the transducer's markers, T , relative to the reference is also known at each frame (Fig. 3).

Therefore if PT_I , the transformation from the image coordinate system, I , to the phantom coordinate system, P , can be found, then TT_I , the transformation from the im-

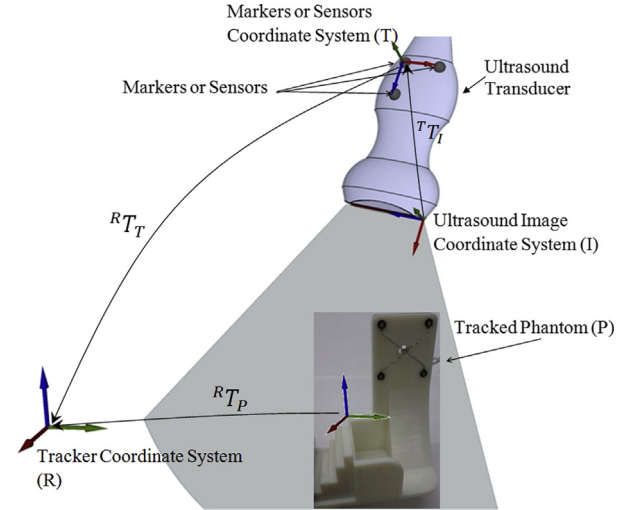


Fig. 3. The coordinate systems defined on the markers' rigid bodies on the transducer, T , and the phantom are measured in the tracker's reference coordinate system, R . The coordinate system of the phantom's wedges, P , relative to the phantom markers is known by the CAD model; therefore, RT_P can be calculated from tracker measurements. RT_T is also measured by the tracker.

age to the transducer coordinate, known as the calibration matrix, can be calculated:

$${}^TT_I = {}^TT_R {}^RT_P {}^PT_I. \quad (1)$$

Solving the calibration transform requires measurement of the transformation from the image coordinate system to the phantom coordinate system, PT_I . We have proposed a new formulation for this problem where we define the image coordinate system with two free vectors, \vec{U} and \vec{V} , as axial and lateral axes, and its origin, P_0 , with respect to the phantom's coordinate system (Fig. 4).

To find the pose of the ultrasound imaging plane, line segment features in the ultrasound image are extracted. The slope and intercept of each of the five lines depend on the pose of the ultrasound imaging plane relative to the phantom. These properties of the line segments can be measured very accurately by the differential measurement technique, as mentioned earlier. A closed-form algorithm has been developed to find the pose of the imaging plane based on these measurements and the given geometric model of the phantom.

Mathematical framework and notations

The multi-wedge calibration phantom can be defined with five different planes. Each plane equation is known from the CAD model. Therefore, the normal vector, n_i , and a point, Q_i , of each plane is known in the phantom coordinate system (Fig. 4). The wedge phantom appears as five line segments in the ultrasound image (dashed lines in Fig. 1).

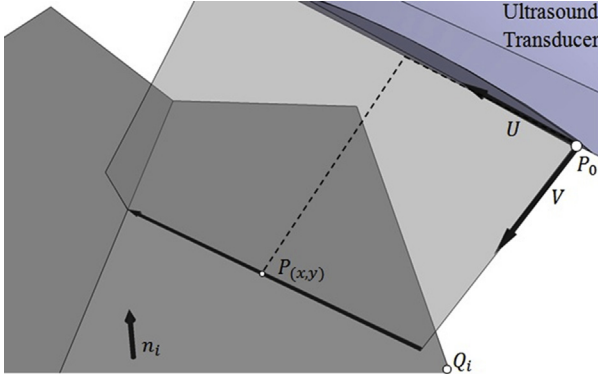


Fig. 4. Intersection of the ultrasound image and the phantom's i th plane. \vec{U} is a unit vector in the direction passing through the center of array elements (lateral), and \vec{V} is a unit vector in the direction of the ultrasound beam (axial). P_0 is the origin of the imaging plane. A plane equation on each wedge (i) is defined with a normal vector, n_i , and a point, Q_i .

As mentioned before, ${}^P T_I$ can be defined from two free vectors, \vec{U} and \vec{V} , and a point, P_0 , where \vec{U} is a unit vector in the direction passing through the center of array elements (lateral), and \vec{V} is a unit vector in the direction of ultrasound beam (axial). P_0 is the origin of the imaging plane in the phantom coordinates.

The solution for ${}^P T_I$ is divided into two stages. First, the rotation matrix (derived from vectors \vec{U} and \vec{V}) and the speed of sound scale, S_y , are solved. Then the translation vector is determined by solving for P_0 .

Rotation parameters

The 3-D representation of each pixel (x_1, y_1) of the image in the phantom coordinate system can be calculated as

$$P = P_0 + S_x x_1 \vec{U} + S_y y_1 \vec{V}. \quad (2)$$

S_x and S_y are pixel-to-milliliter ratios in the lateral and axial directions, respectively. Each line segment, in fact, is the intersection of two planes: the imaging plane and the wedge plane. Therefore, each point on the i th line segment also resides on the i th wedge plane and must satisfy its plane equation (Fig. 4):

$$[P_0 + S_x x_1 \vec{U} + S_y y_1 \vec{V} - Q_i] \cdot \vec{n}_i = 0, \quad (3)$$

$$P_0 \cdot \vec{n}_i + S_x x_1 \vec{U} \cdot \vec{n}_i + S_y y_1 \vec{V} \cdot \vec{n}_i = \underbrace{Q_i \cdot \vec{n}_i}_{d_i}. \quad (4)$$

Considering another point (x_2, y_2) on the same line segment, we have

$$P_0 \cdot \vec{n}_i + S_x x_2 \vec{U} \cdot \vec{n}_i + S_y y_2 \vec{V} \cdot \vec{n}_i = Q_i \cdot \vec{n}_i. \quad (5)$$

Now, subtracting (4) from (5) yields

$$S_x(x_2 - x_1) \vec{U} \cdot \vec{n}_i + S_y(y_2 - y_1) \vec{V} \cdot \vec{n}_i = 0, \quad (6)$$

and then dividing by S_x , we have

$$\Delta x \vec{U} \cdot \vec{n}_i + k \Delta y \vec{V} \cdot \vec{n}_i = 0, \quad (7)$$

where $k = S_y/S_x$, $\Delta x = x_2 - x_1$ and $\Delta y = y_2 - y_1$. Then by dividing eqn (7) by Δx and assuming $m = \Delta y/\Delta x$,

$$\vec{U} \cdot \vec{n}_i + k m_i \vec{V} \cdot \vec{n}_i = 0. \quad (8)$$

In eqn (8), m_i is the slope of the i th line segment (measured by the differential technique), and \vec{n}_i is known from the plane equation for the corresponding wedge. \vec{U} , \vec{V} and k must be solved under the constraint that \vec{U} and \vec{V} are unit vectors. Using at least five linear equations such as (8) (for five independent planes) is sufficient to solve for these unknowns.

One way of deriving \vec{U} and \vec{V} while getting a non-zero value on the right side is by taking a differential measurement from points on two different parallel wedges instead of two points on the same wedge. This means that the second point (x_2, y_2) is on a plane with the same normal vector, n_i , but different right-side constant:

$$P_0 \cdot \vec{n}_i + S_x x_2 \vec{U} \cdot \vec{n}_i + S_y y_2 \vec{V} \cdot \vec{n}_i = d'_i. \quad (9)$$

Now, by subtracting eqn (4) from eqn (9) (instead of eqn [5]), we have

$$S_x(x_2 - x_1) \vec{U} \cdot \vec{n}_i + S_y(y_2 - y_1) \vec{V} \cdot \vec{n}_i = d'_i - d_i, \quad (10)$$

$$\Delta x \vec{U} \cdot \vec{n}_i + k \Delta y \vec{V} \cdot \vec{n}_i = \frac{d'_i - d_i}{S_x}. \quad (11)$$

Combining (11) with (8) into matrix format yields

$$\begin{bmatrix} \Delta x & \Delta y \\ 1 & m_i \end{bmatrix} \begin{bmatrix} \vec{U} \cdot \vec{n}_i \\ k \vec{V} \cdot \vec{n}_i \end{bmatrix} = \begin{bmatrix} \frac{d'_i - d_i}{S_x} \\ 0 \end{bmatrix}, \quad (12)$$

which can be easily solved to obtain $\vec{U} \cdot \vec{n}_i$ and $k \vec{V} \cdot \vec{n}_i$, which are projections of \vec{U} and $k \vec{V}$ on vector n_i . To solve for \vec{U} , \vec{V} and k , we need one more pair of parallel wedges with a different normal vector along with imposing the unity constraint. Complete derivations can be found in [Appendix A](#).

In this approach, two pairs of parallel wedges are used to solve for rotation parameters, but because three wedges with different normal vectors are required for solving translation parameters, one other wedge with a normal vector non-parallel to each of wedge pairs is also needed (a total of five wedges).

The rotation part of ${}^P T_I$ can be determined as

$$R = [X_{3 \times 1} \ Y_{3 \times 1} \ Z_{3 \times 1}], \quad (13)$$

$$X = \vec{U}, \quad (14)$$

$$Z = \frac{X \times \vec{V}}{\|X \times \vec{V}\|}, \quad (15)$$

$$Y = \frac{Z \times \vec{U}}{\|Z \times \vec{U}\|}. \quad (16)$$

Here, we have calculated k , which is the ratio of axial to lateral pixel-to-millimeter ratio. Lateral pixel-to-millimeter ratio is related to the spacing between image columns, which is the spacing of the transducer's elements. This spacing is generally provided by the manufacturer, and for example, for the transducer used in this study it is 0.3 mm. On the other hand, axial pixel-to-millimeter ratio depends on the chosen image formation spacing and the speed of sound. Using the calculated value for k and assuming either S_x or S_y is known, the other one can be calculated. Also, the deviation of the crossing angle between \vec{U} and \vec{V} from 90° can be expressed as the skew angle.

Up to this point, the rotational matrix and speed of sound variation scale are determined from \vec{U} , \vec{V} and k . The derivation of the translation parameters is described next.

Translation parameters

To find the translation part of ${}^P T_I$, P_0 should be calculated. Now looking at (4), d_i and S_x , are known and S_y , \vec{U} and \vec{V} have been determined from the previous step (see Rotation Parameters), so α_i and β_i are also known:

$$P_0 \cdot \underbrace{\vec{n}_i}_{\alpha_i} + S_x x \underbrace{\vec{U} \cdot \vec{n}_i}_{\beta_i} + S_y y \underbrace{\vec{V} \cdot \vec{n}_i}_{d_i} = Q_i' \cdot \vec{n}_i. \quad (17)$$

To solve P_0 , we need to have at least three independent equations as above. Therefore, x and y locations of three points on three wedges with different normal vectors are required. The matrix format for these equations is

$$\begin{bmatrix} \vec{n}_1' \\ \vec{n}_2' \\ \vec{n}_3' \end{bmatrix} P_0 = \begin{bmatrix} d_1 - S_x x \alpha_1 - S_y y \beta_1 \\ d_2 - S_x x \alpha_2 - S_y y \beta_2 \\ d_3 - S_x x \alpha_3 - S_y y \beta_3 \end{bmatrix} = D, \quad (18)$$

$$NP_0 = D. \quad (19)$$

Equation (19) is a linear system of equations and can be easily solved:

$$P_0 = N^{-1}D. \quad (20)$$

Of course it can be solved with more than three points in a least-squares sense to improve accuracy. Now, both the rotation and translation parts of ${}^P T_I$ are known, and the calibration transform (${}^P T_I$) can be found from eqn (1).

Phantom design

In the design of the multi-wedge phantom, a suitable angle of each wedge is chosen so that the line segments are clear in the image and can be segmented accurately; at the same time the slopes are still large enough to achieve low sensitivity of the calibration results to the measurement error.

In fact, it is a design trade-off that can be better understood by explaining RF image formation and the measurement process. An ultrasound image is composed of different columns of envelope-detected RF echo signals. When imaging a flat surface with ultrasound, the RF echo in each column is produced at a certain depth of the image. All of these reflection points reside on a straight line that is the intersection of the imaging plane and the surface (Fig. 5). As long as at least two columns have similar echo signatures, the slope of this line can be measured very accurately (because of the relatively high axial resolution) by determining their axial shift with the normalized cross-correlation technique (Walker and Trahey 1995; Zahiri-Azar and Salcudean 2006).

The signatures of the RF echoes in all the columns will be the same if the ultrasound beam axis is perpendicular to the surface because they all experience the same physical conditions. However, as the angle between the beam axis and the normal of the surface increases, the

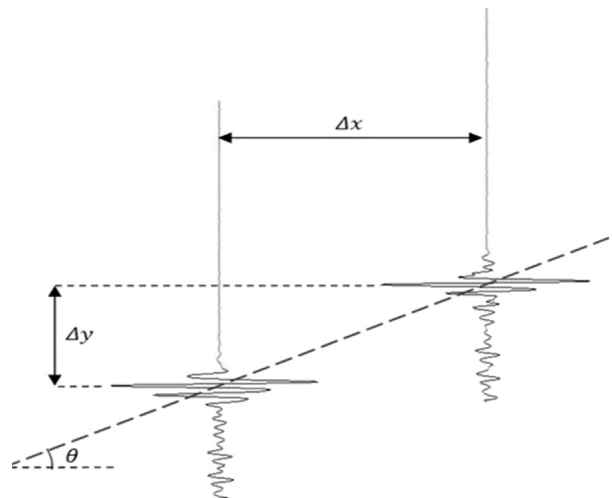


Fig. 5. Slope measurement with radiofrequency cross-correlation: $\tan(\theta) = \Delta y / \Delta x$.

signature of the returned echo slightly changes. This phenomenon occurs because of the anisotropic and spatially variant point-spread function of the ultrasound beam.

Although smaller inclination angles result in lower measurement error, the sensitivity of the calibration estimation to measurement error is very large for such low angles, and this means more difficult parameter identification. The extreme case is an inclination angle of zero, which means all the wedges are parallel and the problem is obviously impossible to solve.

To investigate the effect of wedge inclination on slope measurement error, the RF image of the phantom was simulated using the Field II ultrasound simulation package. The plane was modeled with about 10,000 discrete scatterers and 0.1-mm spacing. The angle between the beam axis and the plane normal was varied while observing the error in the slope measurement. A single focus point at the plane depth (20 mm) was used, and imaging parameters similar to those in the real experiment were used.

Automatic feature extraction and measurement

As described before, five line segment features should be detected in the ultrasound image to perform calibration. In this section, the proposed automatic image processing algorithm is described (Fig. 6). First, a morphologic open operation with line structuring elements was applied to the image. To be able to pick up line segments with different slopes, line structuring elements with different slope values (in this case in the range of -10° to 10° with 5° steps) were used. The results of the opening operation with different structuring elements (after applying a threshold) were combined with a logical disjunction (or) operator into a single binary image. Then a morphologic dilate operation with a disk structuring element was applied to this binary image.

The next step was to remove outlier line segments below the actual surface of the phantom by removing the underlying (noisy) part. For this reason, in each column of the binary image starting from the top, the first segment was kept and the rest of the column was discarded. Thereafter, all the connected regions with a measure of 8-connected neighborhood with no holes were selected. Specific details of the operations and the corresponding MATLAB (The MathWorks, Natick, MA, USA) functions are summarized in Table 1.

Finally, each region was considered as a candidate line segment. A quality check procedure was performed to check for the correct number of line segments. Then, by use of the previously described cross-correlation technique, the slope of each line was calculated from pairs of image columns (B-mode or RF data). After a line was fit to each segment, the middle point, x_i , was taken and its depth, y_i , was automatically measured from the peak of the RF echo. The value of the line depth (related to line intercept) is an absolute measurement with an uncertainty of the exact actual plane-image intersection in the RF signal. Although this value has greater inherent error than differential measurements, the result (translation parameters) is not very sensitive to this measurement (investigated later under Sensitivity analysis to measurement error).

EXPERIMENTS AND RESULTS

In this section, phantom parameter selection is explained followed by evaluation of the success of the automatic segmentation algorithm.

In a set of experiments using both simulated data and experimental data, several evaluation measures were obtained. The sensitivity of the method to measurement error was evaluated using simulated data. Experimental results using different numbers of images of the multi-wedge phantom come next. Calibration precision and

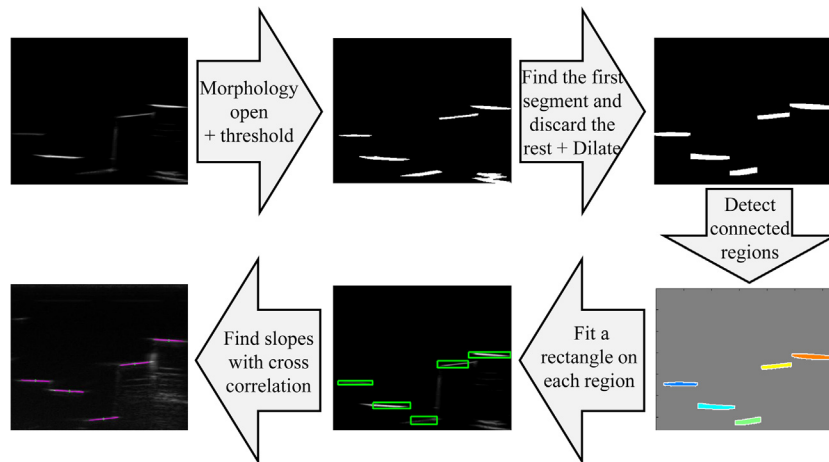


Fig. 6. Automatic feature extraction from the ultrasound image to find the line segments.

Table 1. Specific details of the operations and corresponding MATLAB functions in the image processing procedure

Operation/ attribute	Value	MATLAB command
Image size	340 × 319	—
Morphologic open	LEN = 30	SE = strel (‘line’, LEN, DEG);
Binary threshold	DEG (range) = -10:5:10	IM2 = imopen (IM, SE);
Morphologic dilate	Threshold = MAX/6	—
	R = 3, N = 4	SE = strel (‘disk’, R, N);
Segmentation	conn = 8	IM2 = imdilate (IM, SE);
	options = ‘noholes’	bwboundaries (I, conn, options);

calibration accuracy were measured for the proposed method using either RF or B-mode data and compared with those for the double N-wire method. The method with RF data is referred to as “RF multi-wedge,” and the method with B-mode data is called “B-mode multi-wedge.” The same cross-correlation technique is used to measure the differential distances on the columns of the B-mode images. The peak of the normalized cross-correlation was used as a measure of the similarity of two signals, and the location of the peak gives the relative shift of the two signals. The peak of the normalized cross-correlation was in the range 0.9 to 0.98. Lower values occurred near the edges because of grating and side lobes and possible interference from other wedges. By application of this method on different pairs of scan lines, the value of the slope of each line segment was measured. Then the outliers were removed, and the average of these values was taken.

For the double N-wire method, 100 different images of the double N-wire (integrated into the phantom) were captured and used for calibration. An automatic segmentation algorithm as explained in [Chen et al. \(2009\)](#) was used.

Phantom parameter selection

In the Field II simulation, the angle between the beam axis and the plane normal, ϕ , was chosen in the interval of 0° to 45° . Then the error of cross-correlation-based slope measurement was calculated ([Fig. 7a](#)) by dividing the axial measurement error, error (Δy), by the lateral distance ($\Delta x > 5$ mm for each wedge). Results indicate that as the plane tilts toward higher angles with respect to the ultrasound beam, larger errors in slope measurement are observed. This is because of the change in the echo signature for different columns.

Our observation of the results of a slope measurement experiment when imaging a flat metallic surface immersed in water in different poses also indicate that

as the plane’s inclination angle increases, the line appears thicker in the image and the standard deviation of the slope measurement error increases.

The sensitivity of the system to measurement error was measured with a simulation experiment. In the closed-form mathematical model of the system, the wedge inclination angle, ϕ , was varied over the range 1° to 45° . Axial measurement error was modeled as a random variable with a normal distribution of zero mean and constant standard deviation (10 mm). In 500 iterations, the estimated rotation parameters were compared with true values to calculate the estimation error of the system. Because the level of this output error is dependent on the input (axial) measurement error, the ratio of output to input error is calculated. [Figure 7b](#) illustrates the ratio of the standard deviation of the error in rotation parameters to the standard deviation of the axial measurement error.

As expected, the results indicate that the system is more sensitive to input error at lower angles, and the sensitivity decreases as ϕ increases. We observed that this ratio is not very dependent on the level of measurement error, which means that similar results will be obtained for different values of input error (instead of 10 mm).

According to the results illustrated in [Figure 7a](#) and [b](#), wedges with a 10° inclination angle seem to be a reasonable compromise between maintaining a constant signature (low measurement error) and parameter identification (low sensitivity); hence this value was used in the design of the phantom in this work.

Automatic segmentation evaluation

For calibration, 100 different images of the multi-wedge phantom were acquired and the automatic feature extraction algorithm was applied to them.

The number of line segments detected in the image is a measure of the algorithm’s performance. In 88 images, 5 line segments were correctly detected. In the other images, 4, 6 and, in one case, 3 line segments were detected. The frequency distribution of the number of detected line segments is provided in [Table 2](#).

Sensitivity analysis to measurement error

To estimate the sensitivity of the method to measurement error, the calibration process was simulated. The simulation helps us to understand how measurement error propagates into the calibration matrix. In this simulation experiment, axial measurement error (e) was modeled as a random variable with a normal distribution of zero mean and standard deviation varying from 1 to 50 μm . Note that at a 40-MHz sampling rate, the RF sample interval is 20 μm . Means and standard deviations of the calibration parameters were calculated (1000 iterations). The

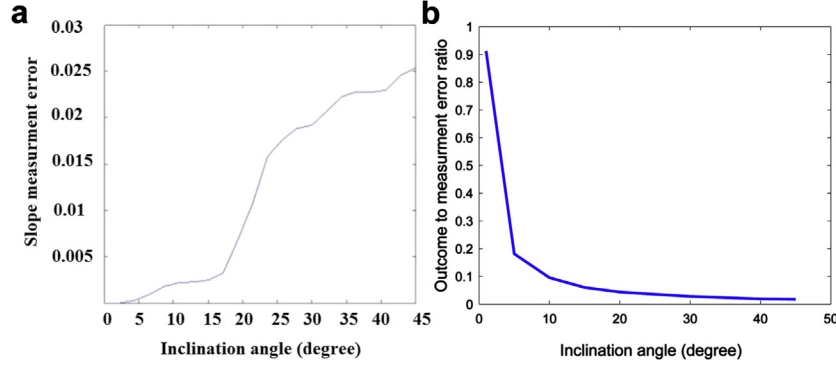


Fig. 7. (a) Slope measurement error, error $(\Delta y)/\Delta x$, versus inclination angle, ϕ . (b) Ratio of outcome (absolute sum of rotation angles) error to measurement error ($^{\circ}/\text{mm}$) for different inclination angles (ϕ).

Euclidean norm of the means and the standard deviations for each of the translation and rotation vectors were calculated and are illustrated in Figure 8.

Calibration experimental results

Calibration parameters were calculated using different numbers of images. In each pose, the transducer was fixed with a mechanical arm while acquiring the ultrasound image and capturing the tracking information. We ensured that all the five wedges were clearly visible in the ultrasound image and that the phantom was scanned from all possible positions and angles. To minimize tracking error, the tracking information was averaged for each pose. For all the images, the imaging depth and focus were set to 4 and 2 cm, respectively.

Each time, n_s ($= 2-87$) images were randomly chosen from all the 88 segmented images, and the calibration parameters were calculated. The rotation matrix was decomposed into yaw, pitch and roll angles (a , b , g) as follows:

$$R = R_z(\alpha)R_y(\beta)R_x(\gamma). \quad (21)$$

For each set of n_s images, the calibration solution was derived independently and the average of calibration parameters has been taken. The number of combinations of selecting n_s images out of 88 is fairly large except for $n_s = 1$. Therefore, in 250 iterations, n_s images were randomly selected from the data set. The standard deviation and the average of the results were calculated and are illustrated in Figure 9. These results indicate that the standard deviation of the error rapidly decreases as the number of input images increases. A relatively small number

of images are sufficient to achieve accurate results. Note that given the closed-form nature of the solution, the order of the images is unimportant.

Figure 9 illustrates that in-plane rotation (α) can be determined with more precision compared with out-of-plane rotations (β and γ). The reason is that compared with pitch and roll angles, a variation in the yaw angle causes a larger change in the image features (slopes). This rotation error propagates to translation parameters and results in relatively larger error in t_z . This is an inevitable effect of a 2-D imaging modality which affects other 2-D calibration methods as well (*e.g.*, Fig. 11 in Chen et al. [2009]).

Calibration precision

One way to measure calibration precision is by determining the variability in the reconstruction position of points in the image using different calibration solutions. In this approach, a certain point in the image (*e.g.*, bottom right corner) is reconstructed using different calibration solutions, and the variation is measured. There is no need for imaging a phantom, and therefore, alignment and segmentation errors are not involved. Moreover, the reconstruction can be performed in the marker's coordinate system rather than the reference coordinate system; hence the tracking error can also be eliminated (Hsu et al. 2008). This approach is also known as calibration reproducibility (CR) and is defined as

$$\mu_{\text{CR}} = \frac{1}{N} \sum_{i=1}^N \left| {}^p T_{l_i} p^I - \overline{p^I} \right|, \quad (22)$$

where T_{l_i} is any of N calibration solutions, p^I is an arbitrary point in image coordinates and $\overline{p^I}$ is the average of the transformed point in the transducer coordinate system.

Here, the CR test was performed on both the multi-edge and double N-wire methods for different numbers n_s

Table 2. Frequency distribution of the number of detected line segments in 100 ultrasound images

Number of line segments	3	4	5	6
Count of the occurrences	1	10	88	1

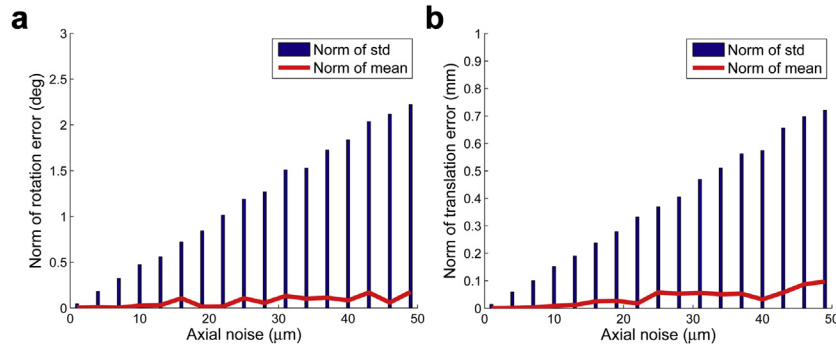


Fig. 8. Sensitivity analysis of radiofrequency multi-wedge to axial measurement error. (a) Norm of rotation error vector (mean and standard deviation). (b) Norm of translation error vector (mean and standard deviation). std = standard deviation.

of images. For each n_s ($= 2-86$), in 200 iterations ($N = 200$), the calibration matrix was computed for n_s randomly chosen images from the data collection. The variability of the top left ($p^l = [0, 0, 0]$ mm) and the right bottom ($p^r = [38, 40, 0]$ mm) points was computed and averaged over all the iterations. m_{CR} values for top-left and bottom-right corner points are depicted in Figure 10.

Calibration accuracy

In the PRA test, probably the most objective measure of accuracy, a point is scanned and its location reconstructed in 3-D space using the calculated calibration matrix (Hsu et al. 2008). The true 3-D location of the point phantom is determined by a tracked stylus. This test was performed using a stylus (NDI 4-marker probe).

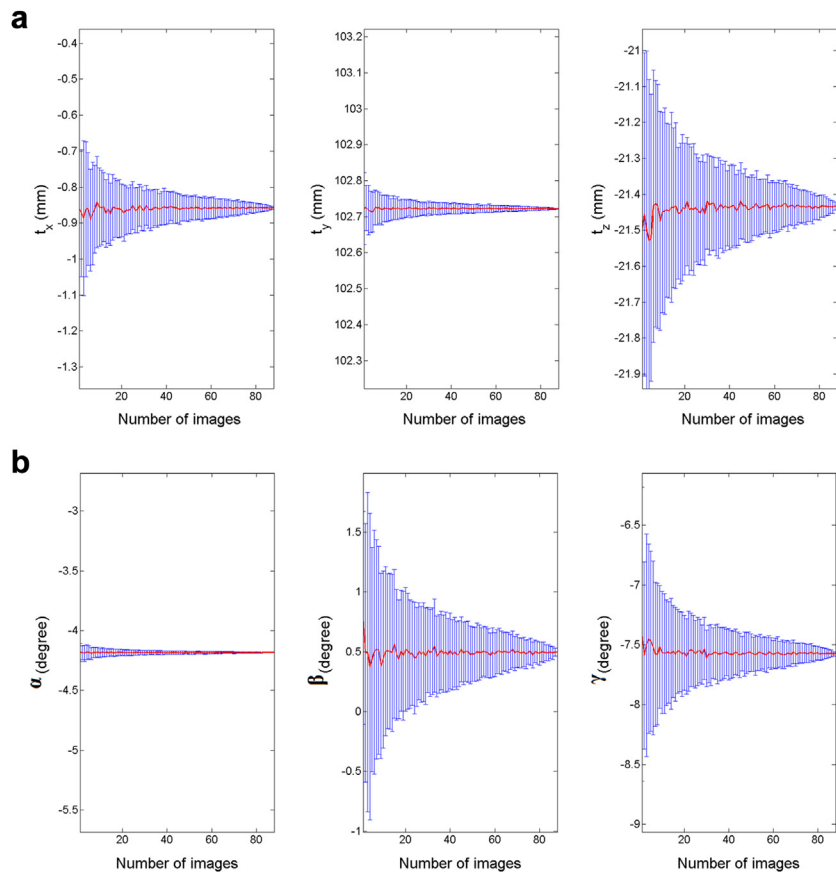


Fig. 9. Calibration results of the radiofrequency multi-wedge method using 2 to 87 images of the phantom. Means (red) and standard deviations (blue) of (a) translation parameters (t_x, t_y, t_z) (mm) and (b) rotation parameters (a, b, g) ($^\circ$) are illustrated.

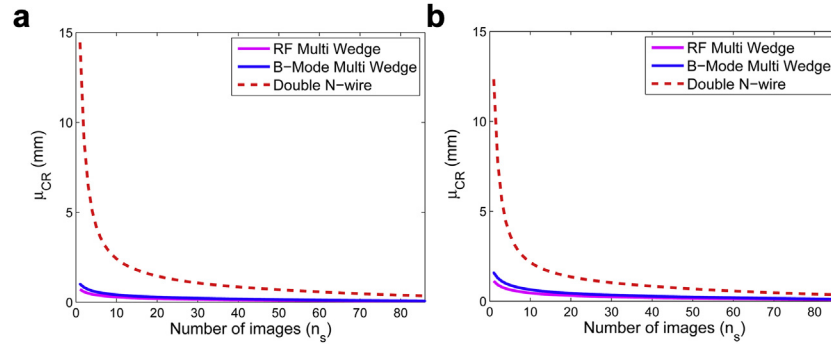


Fig. 10. Calibration reproducibility (CR) measure of calibration parameters when using different number of images, n_s , for the (a) top left corner point and (b) bottom right corner point. RF = radiofrequency.

The stylus was precalibrated by the manufacturer, but was also calibrated by the pivot procedure in the NDI software. The reported accuracy was 0.15-mm 3-D root mean square error and 0.1-mm mean error. To confirm the results, a planar phantom was created with a 3-D printer comprising a grid of 3×4 semi-spherical holes on the surface with 30-mm spacing. The distances between the holes were measured using the stylus. The size of the holes was the same as the stylus bead to make sure it remained fixed at each point. The stylus was positioned at different angles during this experiment. In a total of 17 measurements between adjacent points in both directions, the error was 0.07 ± 0.13 mm.

The stylus was affixed in a water bath, and the transducer was placed in 65 different positions. In each position, the transducer was aligned carefully in such a way that the stylus bead would be clearly seen in the ultrasound image. This test was performed over an extended imaging depth of 5.5 cm (compared with a 4-cm imaging depth for calibration). The stylus was positioned at different angles and different depths of the image. The stylus bead was manually segmented in ultrasound images by fitting a circle with a known radius to the bead image. To minimize tracking error, the average of the tracking information was taken for both the transducer and the stylus at each pose while they were both fixed. The Euclidian distance error is calculated for the

65 images for all the methods and summarized in Table 3. The average point reconstruction error for the “RF multi-wedge” method was 0.09 ± 0.39 mm. The range of skew angles is small, $\pm 0.5^\circ$.

CONCLUSIONS

In this article, we proposed a novel closed-form method for freehand 3-D ultrasound calibration that extends previous calibration techniques. The method was developed based on the specific physical properties of ultrasound imaging system. The relative shift of two RF echo pulses hitting the same plane surface seems to be a very accurate measure on which to base a calibration technique. With this in mind, based on the simulations and the experiments, a multi-wedge phantom has been proposed. There is a trade-off in the design of the phantom. For a given measurement error, the calibration error decreases as the surfaces in the phantom become steeper and more distanced from each other, but on the other hand, the measurement error for those surfaces increases.

Experimental results indicate that the method is very precise. The CR test indicates that using only a single image of the phantom is almost as precise as using 50 images of a double N-wire phantom. Results of the calibration accuracy evaluation using the PRA test confirm that the proposed method has higher accuracy compared with the double N-wire method (Chen *et al.* 2009). However, it should be noted that the PRA test includes all the errors in the tracking and imaging process such as alignment, segmentation and tracking errors, which makes it challenging to judge and compare the results, especially when reaching sub-millimeter levels of error.

The calibration can be performed in real time using the automatic image processing method; therefore, the calibration will take less than 1 min.

Future work will focus on intra-operative calibration. The phantom can be enclosed in a sterile fluid-filled rubber-topped box for intra-operative use. Because

Table 3. Calibration point reconstruction accuracy test results for three different calibration methods using a stylus (65 points)

Method	Double N-wire		B-mode multi-wedge		RF multi-wedge	
	Mean	SD	Mean	SD	Mean	SD
Distance error (mm)						
Top (10–25 mm)	0.48	0.50	0.26	0.45	0.16	0.46
Center (25–40 mm)	0.18	0.39	0.16	0.38	0.08	0.37
Bottom (40–55 mm)	0.42	0.44	0.32	0.39	0.24	0.38
Average	0.25	0.43	0.18	0.40	0.09	0.39

RF = radiofrequency; SD = standard deviation.

very few images, or even a single image, are required for calibration, the transducer can be fixed into a mechanical slide to capture the images in a fast sweep. This is also helpful in acquiring high-quality images of the phantom with a clear depiction of all the wedges. In fact, when the transducer is tilted more than 20° , the error increases rapidly (Fig. 7a).

Future work will also extend this method to curvilinear and 3-D transducers. Given that the phantom could be easily and inexpensively manufactured using a 3-D printer, this calibration method can be disseminated to a wide range of researchers by sharing CAD files and program code. We are currently integrating the software into the PLUS library (Lasso et al. 2012) for public use.

Acknowledgments—This work is supported by the Natural Sciences and Engineering Research Council of Canada (Grant number RGPIN-239046-10) and Canadian Institutes of Health Research.—The automatic N-wire segmentation was performed using a MATLAB GUI written by Jeff Abeysekera, University of British Columbia.

REFERENCES

- Afsham N, Chan K, Pan L, Tang S, Rohling RN. Alignment and calibration of high frequency ultrasound (HFUS) and optical coherence tomography (OCT) 1 D transducers using a dual wedge-tri step phantom. *Proc SPIE* 2011;7964.
- Amin D, Kanade T, Jaramaz B, DiGioia Anthony M.I, Nikou C, LaBarca R, Moody JE. Calibration method for determining the physical location of the ultrasound image plane. In: Niessen W, Viergever M, eds. *Proceedings, Medical Image Computing and Computer-Assisted Intervention (MICCAI 2001)*. Lecture Notes Comput Sci 2001; 2208:940–947.
- Bergmeir C, Seitel M, Frank C, Simone R, Meinzer H, Wolf I. Comparing calibration approaches for 3-D ultrasound probes. *Int J Comput Assist Radiol Surg* 2009;4:203–213.
- Blackall J, Rueckert D, Maurer C.R. J, Penney G, Hill D, Hawkes D. An image registration approach to automated calibration for freehand 3D ultrasound. In: Delp S, DiGoia A, Jaramaz B, eds. *Proceedings, Medical Image Computing and Computer-Assisted Intervention (MICCAI 2000)*. Lecture Notes Comput Sci 2000;1935:462–471.
- Boctor E, Viswanathan A, Choti M, Taylor RH, Fichtinger G, Hager G. A novel closed form solution for ultrasound calibration. In: *Proceedings, IEEE International Symposium on Biomedical Imaging: Nano to Macro*, Arlington, Virginia, USA, 15–18 April 2004. New York: IEEE; 2004. p. 527–530.
- Boctor EM, Iordachita I, Choti MA, Hager G, Fichtinger G. Bootstrapped ultrasound calibration. *Stud Health Technol Informatics* 2006a; 119:61–66.
- Boctor EM, Iordachita I, Fichtinger G, Hager GD. Ultrasound self-calibration. *Proc SPIE* 2006b;6141.
- Brendel B, Winter S, Erment H. A simple and accurate calibration method for 3-D freehand ultrasound. *Biomed Tech* 2004;49:872–873.
- Chen TK, Thurston AD, Ellis RE, Abolmaesumi P. A real-time freehand ultrasound calibration system with automatic accuracy feedback and control. *Ultrasound Med Biol* 2009;35:79–93.
- Detmer PR, Bashein G, Hodges T, Beach KW, Filer EP, Burns DH, Strandness DE. 3-D ultrasonic image feature localization based on magnetic scanhead tracking: in vitro calibration and validation. *Ultrasound Med Biol* 1994;20:923–936.
- Eggert D, Lorusso A, Fisher R. Estimating 3-D rigid body transformations: A comparison of four major algorithms. *Mach Vision Appl* 1997;9:272–290.
- Gee AH, Houghton NE, Treece GM, Prager RW. A mechanical instrument for 3-D ultrasound probe calibration. *Ultrasound Med Biol* 2005;31:505–518.
- Hsu PW, Prager RW, Gee AH, Treece GM. Freehand 3-D ultrasound calibration: A review. *Adv Imaging Biol Med* 2009;47–84.
- Hsu P, Treece G, Prager R, Houghton N, Gee A. Comparison of freehand 3-D ultrasound calibration techniques using a stylus. *Ultrasound Med Biol* 2008;34:1610–1621.
- Khamene A, Sauer F. A novel phantom-less spatial and temporal ultrasound calibration method. In: Duncan J, Gerig G, eds. In: *Proceedings, Medical Image Computing and Computer-Assisted Intervention (MICCAI 2005)*. Lecture Notes Comput Sci 2005;3750: 65–72.
- Lange T, Kraft S, Eulenstein S, Lamecker H, Schlag P. Automatic calibration of 3-D ultrasound probes. *Bildverarbeitung Med* 2011;2011: 169–173.
- Lasso A, Heffter T, Pinter C, Ungi T, Fichtinger G. Implementation of the PLUS open-source toolkit for translational research of ultrasound-guided intervention systems. In: *Proceedings, Medical Image Computing and Computer-Assisted Intervention (MICCAI 2012)—Systems and Architectures for Computer Assisted Interventions*. MIDAS J The 2012;1–12.
- Lindseth F, Tangen GA, Langø T, Bang J. Probe calibration for freehand 3-D ultrasound. *Ultrasound Med Biol* 2003;29:1607–1623.
- Melvær E, Mørken K, Samset E. A motion constrained cross-wire phantom for tracked 2D ultrasound calibration. *Int J Comput Assist Radiol Surg* 2011;1–10.
- Mercier L, Lang T, Lindseth F, Collins DL. A review of calibration techniques for freehand 3-D ultrasound systems. *Ultrasound Med Biol* 2005;31:449–471.
- Muratore DM, Galloway RL. Beam calibration without a phantom for creating a 3-D freehand ultrasound system. *Ultrasound Med Biol* 2001;27:1557–1566.
- Najafi M, Afsham N, Abolmaesumi P, Rohling R. A closed-form differential formulation for ultrasound spatial calibration. In: Abolmaesumi P, Joskowicz L, Navab N, Jannin P, eds. *Information Processing in Computer-Assisted Interventions*. Lecture Notes Comput Sci 2012a;7330:44–53.
- Najafi M, Afsham N, Abolmaesumi P, Rohling R. Single wall closed-form differential ultrasound calibration. *Proc SPIE* 2012b; 8316.
- Najafi M, Rohling R. Single camera closed-form real-time needle trajectory tracking for ultrasound. *Proc SPIE* 2011;7964.
- Pagoulatos N, Haynor D, Kim Y. A fast calibration method for 3-D tracking of ultrasound images using a spatial localizer. *Ultrasound Med Biol* 2001;27:1219–1229.
- Peterhans M, Anderegg S, Gaillard P, Oliveira-Santos T, Weber S. A fully automatic calibration framework for navigated ultrasound imaging. In: 2010 IEEE Annual International Conf Proc IEEE Eng Med Biol Soc 2010;2010:1242–1245.
- Prager RW, Rohling RN, Gee AH, Berman L. Rapid calibration for 3-D freehand ultrasound. *Ultrasound Med Biol* 1998;24:855–869.
- Trobaugh J, Richard W, Smith K, Bucholz R. Frameless stereotactic ultrasonography: Method and applications. *Comput Med Imaging Graphics* 1994;18:235–246.
- Walker WF, Trahey GE. A fundamental limit on delay estimation using partially correlated speckle signals. *IEEE Trans Ultrason Ferroelectr Freq Control* 1995;42:301–308.
- Yaniv Z, Foroughi P, Kang H, Boctor E. Ultrasound calibration framework for the image-guided surgery toolkit (IGSTK). *Proc SPIE* 2011;7964.
- Zahiri-Azar R, Salcudean SE. Motion estimation in ultrasound images using time domain cross correlation with prior estimates. *IEEE Trans Biomed Eng* 2006;53:1990–2000.

APPENDIX A

This section describes how to solve for \vec{U} , \vec{V} and k from the projections of \vec{U} and $k\vec{V}$ on \vec{n}_i vectors ($\vec{U} \cdot \vec{n}_i$ and $k\vec{U} \cdot \vec{n}_i$). We need these projected values for at least two different values of \vec{n}_i . First, we find \vec{U} using two projection values of it over \vec{n}_1 and \vec{n}_2 :

$$\vec{U} \cdot \vec{n}_1 = u_1, \vec{U} \cdot \vec{n}_2 = u_2. \quad (\text{A1})$$

One more projection of \vec{U} over another vector (e.g., \vec{g}) non-parallel to \vec{n}_1 and \vec{n}_2 is enough to find \vec{U} . This means that we have

$$\begin{bmatrix} \vec{n}_1^t \\ \vec{n}_2^t \\ \vec{g}^t \end{bmatrix}_{3 \times 3} \vec{U} = \begin{bmatrix} u_1 \\ u_2 \\ u_3 \end{bmatrix}, \quad (\text{A2})$$

$$\vec{U} = \begin{bmatrix} \vec{n}_1^t \\ \vec{n}_2^t \\ \vec{g}^t \end{bmatrix}_{3 \times 3}^{-1} \begin{bmatrix} u_1 \\ u_2 \\ u_3 \end{bmatrix}. \quad (\text{A3})$$

This looks like another pair of parallel wedges with normal vector \vec{g} is needed, but in fact it is possible to solve the problem using only \vec{n}_1 and \vec{n}_2 by defining \vec{g} as a combination of them and also using the unity constraint for \vec{U} :

$$\vec{g} = \vec{n}_1 \times \vec{n}_2. \quad (\text{A4})$$

To find the projection of \vec{U} over \vec{g} , u_3 , we define another vector, \vec{f} , which is perpendicular to both \vec{g} and \vec{n}_1 :

$$\vec{f} = \vec{g} \times \vec{n}_1 = (\vec{n}_1 \times \vec{n}_2) \times \vec{n}_1 = \vec{n}_2 - (\vec{n}_1 \cdot \vec{n}_2) \vec{n}_1. \quad (\text{A5})$$

The projection of \vec{U} over \vec{f} can be calculated from

$$\vec{U} \cdot \vec{f} = \vec{U} \cdot \vec{n}_2 - (\vec{n}_1 \cdot \vec{n}_2) \vec{U} \cdot \vec{n}_1 = u_2 - (\vec{n}_1 \cdot \vec{n}_2) u_1. \quad (\text{A6})$$

Because \vec{n}_1 , \vec{g} and \vec{f} are all perpendicular to each other ($\vec{n}_1 \perp \vec{g} \perp \vec{f}$), they form an orthogonal basis, and therefore, \vec{U} can be written as a linear combination of them:

$$\vec{U} = u_1 \vec{n}_1 + u_3 \frac{\vec{g}}{\|\vec{g}\|^2} + (\vec{U} \cdot \vec{f}) \frac{\vec{f}}{\|\vec{f}\|^2}. \quad (\text{A7})$$

Now, by applying the unity constraint for \vec{U} , we have

$$\|\vec{U}\|^2 = \vec{U} \cdot \vec{U} = u_1^2 + \frac{u_3^2}{\|\vec{g}\|^2} + \frac{(\vec{U} \cdot \vec{f})^2}{\|\vec{f}\|^2} = 1, \quad (\text{A8})$$

And finally u_3 can be calculated from

$$u_3 = \pm \|g\| \sqrt{1 - u_1^2 - \frac{(\vec{U} \cdot \vec{f})^2}{\|\vec{f}\|^2}}. \quad (\text{A9})$$

The sign ambiguity should be resolved based on the approximate estimation of the calibration matrix given the geometry of the setup. Now that u_3 is known, it is possible to find \vec{U} using eqn (A3).

Now that \vec{U} is solved, we can solve for \vec{V} and k using eqn (11) for each pair of parallel wedges and using eqn (8) for the fifth wedge:

$$(\Delta x)_1 \vec{U} \cdot \vec{n}_1 + k(\Delta y)_1 \vec{V} \cdot \vec{n}_1 = \frac{d'_1 - d_1}{S_x}, \quad (\text{A10})$$

$$(\Delta x)_2 \vec{U} \cdot \vec{n}_2 + k(\Delta y)_2 \vec{V} \cdot \vec{n}_2 = \frac{d'_2 - d_2}{S_x}, \quad (\text{A11})$$

$$\vec{U} \cdot \vec{n}_3 + km_3 \vec{V} \cdot \vec{n}_3 = 0. \quad (\text{A12})$$

These three equations can be represented by the matrix equation

$$k \begin{bmatrix} \vec{V} \cdot \vec{n}_1 \\ \vec{V} \cdot \vec{n}_2 \\ \vec{V} \cdot \vec{n}_3 \end{bmatrix} = \begin{bmatrix} \left(\frac{d'_1 - d_1}{S_x} - (\Delta x)_1 \vec{U} \cdot \vec{n}_1 \right) / (\Delta y)_1 \\ \left(\frac{d'_2 - d_2}{S_x} - (\Delta x)_2 \vec{U} \cdot \vec{n}_2 \right) / (\Delta y)_2 \\ - (\vec{U} \cdot \vec{n}_3) / m_3 \end{bmatrix} = \vec{b}, \quad (\text{A13})$$

which can be solved to find $\vec{V}' = k \vec{V}$:

$$\vec{V}' = k \vec{V} = \begin{bmatrix} \vec{n}_1^t \\ \vec{n}_2^t \\ \vec{n}_3^t \end{bmatrix}^{-1} \times \vec{b}. \quad (\text{A14})$$

This formulation gives both \vec{V} and k from \vec{V}' simply as its norm and its normalized vector:

$$k = \|\vec{V}'\|, \quad \vec{V} = \frac{\vec{V}'}{k}. \quad (\text{A15})$$